

Characteristics of Non-metallic Inclusions in Steel Obtained from Different-Sized Samplers



HANG LIAO, SHUFENG YANG, JINGSHE LI, and JIE FENG

To determine the effect of sampler size on the detection of inclusions in liquid steel, four different-sized samplers were designed for industrial sampling from a continuous casting tundish. The samples were evaluated *via* scanning electron microscopy and energy-dispersive spectroscopy. With increasing sample size, the cooling rate of the sample and velocity for particle engulfment decreased. The extent of encapsulation of complex inclusions increased from 0 pct with the smallest sampler to 48.2 pct with the largest sampler. In the samplers that cooled at 41.2 and 26.7 K s⁻¹, the major inclusions were calcium aluminates; in the larger samplers, which cooled more slowly at 8.2 and 1.0 K s⁻¹, the complex inclusions predominately comprised Al₂O₃ + (Ca, Mn)S and Al₂O₃ + CaS, respectively. The sizes of the sulfides gradually increased with increasing sampler size; for example, the sulfide average diameter increased from 2.5 to 3.5 μm when the sampler inner diameter increased from 50 to 70 mm. The main direction of movement of the inclusions during the sampling process was upward.

DOI: 10.1007/s11663-017-1085-7

© The Minerals, Metals & Materials Society and ASM International 2017

I. INTRODUCTION

IN steel production, analysis of molten steel is essential for identifying sources of problems that occur during the refining process or for determining its elemental composition; however, there are many sizes of samplers, the choice of which directly influences the cooling rate of steel solidification.^[1–7] The solidification and cooling rates, in turn, affect the size and chemistry of non-metallic inclusions and the accuracy of the inclusion analysis. Selection of an appropriately sized sampler is therefore vital to performing an accurate study of inclusion characteristics.

Several previous studies have investigated the influence of sampler type on inclusion behavior during the sampling process. Some studies found that the filling velocity and solidification of liquid steel were dependent on the sampler geometry and that the steel composition affected the distribution and size of inclusions.^[8,9] Compared with inclusions obtained by metal-cap-protected lollipop-shaped samplers, most inclusions in argon-protected lollipop-shaped samplers were distributed more homogeneously which resulted in lower and more even filling velocities.^[8] Zhang *et al.*^[10] found

that the predicted inclusion collisions due to turbulence during sampling were much higher than those that occurred in a ladle furnace during steelmaking. In lollipop-shaped samplers, the bottom half is preferred region for analysis, except for areas close to the bottom surface.^[11] Barrel-type samplers are also used in industrial experiments; these are not prone to the formation of shrinkage voids in the sample because of a steady filling velocity during the sampling process.^[12,13]

Using current technologies, direct observation of changes in inclusions during the solidification process is impossible; factors affecting the characteristics of inclusions during the solidification have therefore been investigated using various analysis methods. Ma *et al.*^[14–17] used a segregation model and nucleation theory to investigate the precipitation and growth of inclusions during the solidification process. Goto *et al.*^[18–20] determined the characteristics of inclusions during solidification by comparing the oxygen content and cooling rate of different types of steels. In laboratory experiments, Ohta^[21] used the change in Ni content of different regions of the steel sample to identify different stages of solidification; in this way, the effects of various elements on inclusion characteristics during solidification were determined. In summary, most of the aforementioned studies were based on laboratory experiments and theoretical analyses to study the characteristics of inclusions during solidification. Few studies of the effects of different-sized samplers have been performed on an industrial scale.

In the present work, four different-sized barrel-shaped samplers with wooden covers were designed for

HANG LIAO, SHUFENG YANG, JINGSHE LI, and JIE FENG are with the School of Metallurgical and Ecological Engineering, University of Science and Technology Beijing, Beijing 100083, China. Contact e-mail: yangshufeng@ustb.edu.cn

Manuscript submitted August 30, 2016.

Article published online September 14, 2017.

industrial experiments in a continuous casting tundish. The steel samples collected were evaluated *via* scanning electron microscopy (SEM) and energy-dispersive spectroscopy (EDS). This allowed examination of non-metallic inclusions in steel that had solidified and cooled at different rates in the different-sized samplers. The influence of cooling rate on the size of the sulfide inclusions was determined by comparing the average size of these inclusions in steel samples of different sizes.

II. MATERIALS AND EXPERIMENTAL METHODS

A. Sampler Design

The shape of the sampler is shown in Figure 1. The sampling mold was made of 1045 steel. A wooden cover was placed on the top of each sampler to prevent slag from entering the bottom of the sampler before sampling. To ensure that the thicknesses at the bottom and side were the same, the height of the sampler was changed proportionally to the inner diameter to obtain four samplers with distinct sizes. The parameters of the different-sized samplers are listed in Table I.

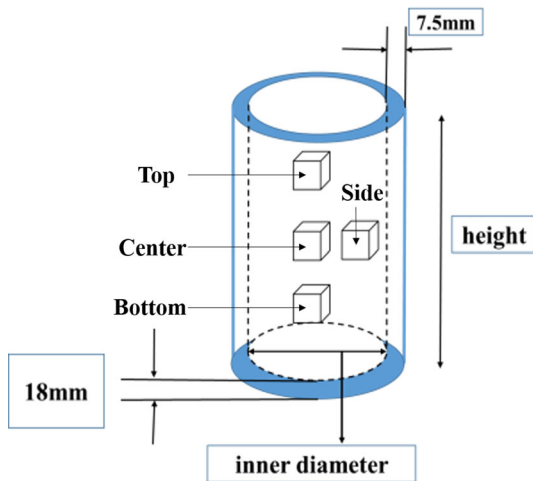


Fig.1—Schematic of sampler design and locations of steel samples used for analysis.

Table I. Parameters of Different-Sized Samplers

Group	Inner Diameter/mm	Height/mm
1	20	62
2	30	88
3	50	134
4	70	182

Table II. Chemical Compositions of 42CrMo Steels from Three Heats (in Mass Percent)

Heat	C	Si	Mn	Cr	Mo	S
6E112	0.43	0.2644	0.5720	0.9539	0.1705	0.0021
6E113	0.42	0.2465	0.5714	0.937	0.1666	0.0021
6D112	0.42	0.2391	0.5559	0.9367	0.1668	0.0022

B. Industrial Experiments

The chemical composition of the 42CrMo steel used in this study is shown in Table II.

A total of three industrial experiments was performed in the casting tundish (casting time: 20–25 minutes), designated as 6E112, 6E113, and 6D112. The sampling requirements were as follows: (1) each experiment was performed with four groups of different-sized samplers; (2) in each group, two samplers of the same size were used to sample simultaneously; (3) to ensure that the temperature of the molten steel was fixed, the four groups of samplers were used to sample continuously during each experiment; (4) all of the samples were cooled in air. Figure 2 shows the samples after cooling. Eight samples were obtained from each experiment.

Each barrel-shaped sampler was connected to a long iron rod by welding; this was used to insert the sampler into the tundish bath. The iron rod was about 1.5 m in length to ensure that the sampling location was far below the level of the slag. Each sampler was kept in the tundish for about 2–3 seconds and then removed and quenched in the air.

C. Sample Analysis

Samples of the cooled steel were taken at the top (1/4 height), center (1/2 height), bottom (3/4 height), and side (1/2 height and 1/4 radial direction) positions of the samplers with inner diameters of 50 and 70 mm (see Figure 1). Because the volumes of liquid steel in the samplers with inner diameters of 20 and 30 mm were small, samples were not taken from the sides of the samplers. The samples were machined into $15 \times 15 \times 15$ mm³ blocks and polished. The center samples were used to determine the cooling rate by measuring the secondary dendrite arm spacing. The steel samples were etched with picric acid solution at 333 K (60 °C) for 2–5 minutes prior to analysis.

Ten photographs of each steel sample were taken using a PhenomTM Pro X scanning electron microscope (Netherlands) to reveal the dendritic structure of the steel; the secondary dendrite arm spacing was measured and a mean value calculated for each sample.^[22] In addition, the inclusions present in the different steel samples were evaluated by SEM and EDS to determine their morphologies and compositions. The inclusions in 50 consecutive fields were observed at an SEM magnification of $\times 1500$ and their size, type, and quantity were determined. The encapsulation rate of duplex inclusions is defined as x , which was calculated according to

$$x \text{ pct} = \frac{N_f}{N} \times 100, \quad [1]$$

where N_f (mm^{-2}) is the total number of duplex inclusions per unit area that were classified as encapsulated inclusions and N (mm^{-2}) is the total number of inclusions per unit area.

III. RESULTS AND DISCUSSION

A. Cooling Rate of Different-Sized Samples

When the carbon content in a steel is <0.53 pct, the dependence of the secondary dendrite arm spacing on the cooling rate of the steel is determined from [23]

$$\lambda_2 = 148C_R^{-0.38}, \quad [2]$$

where λ_2 (μm) is the secondary dendrite arm spacing and C_R (K s^{-1}) is the cooling rate.

The measured secondary dendrite arm spacing and the calculated cooling rates of different-sized samples are listed in Table III. The cooling rate gradually decreased with increasing sample size. The cooling rates for the samplers with inner diameters of 20, 30, 50, and 70 mm were, respectively, 41.2, 26.7, 8.2, and 1.0 K s^{-1} .

B. Change in Extent of Encapsulation of Inclusions

Oxide-sulfide duplex inclusions, in which the oxide was combined with a sulfide located at some or all of its periphery, represented the major type of complex inclusion found in this study. Figure 3 shows the morphologies of inclusions in the different-sized steel samples: oxide and sulfide inclusions occur in the dark and light shades, respectively. The cooling rate of the samples gradually decreased with increasing sample size



Fig.2—Different-sized samples after cooling.

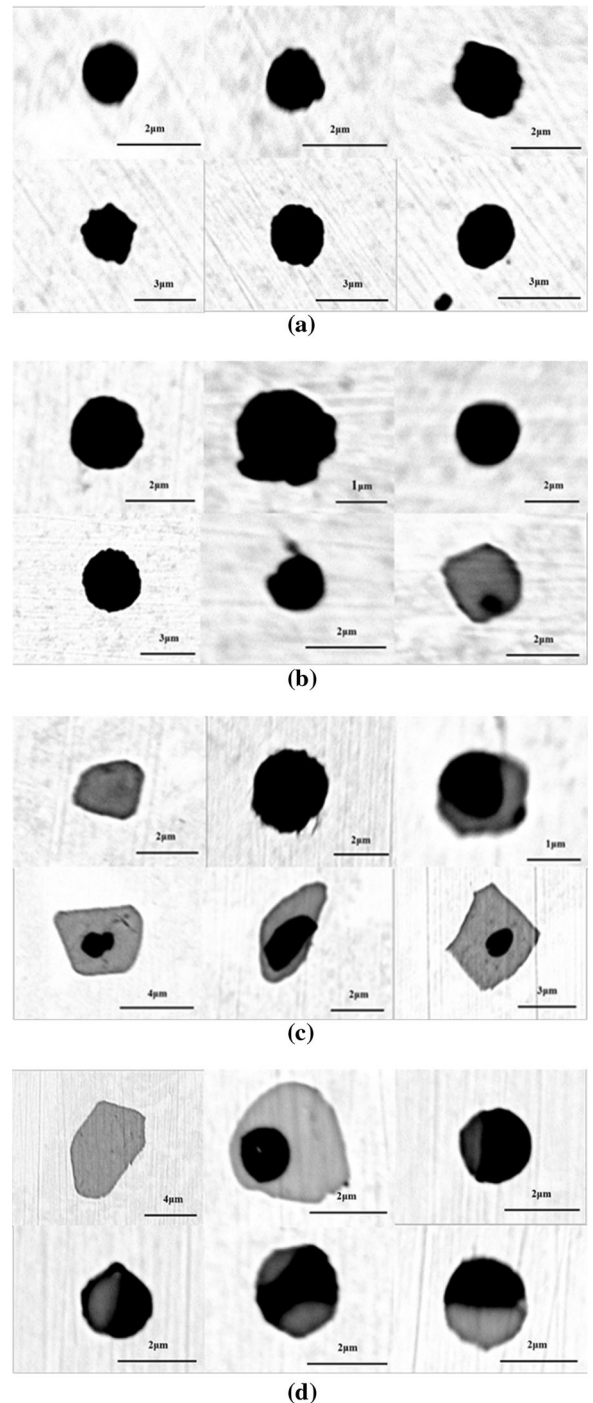


Fig.3—Morphology of inclusions in steel samples taken with sampler diameters of (a) 20 mm, (b) 30 mm, (c) 50 mm, and (d) 70 mm.

Table III. Secondary Dendrite Arm Spacing, Cooling Rates, and Solidification Front Velocity of Different-Sized Samples

Group	Inner Diameter/mm	Average Secondary Dendrite Arm Spacing/ μm	Cooling Rate/ K s^{-1} (deg/s)	Solidification Velocity/ K s^{-1} (deg/s)
1	20	36.04	41.2	3.7
2	30	42.44	26.7	2.8
3	50	66.67	8.2	1.4
4	70	83.14	1.0	0.2

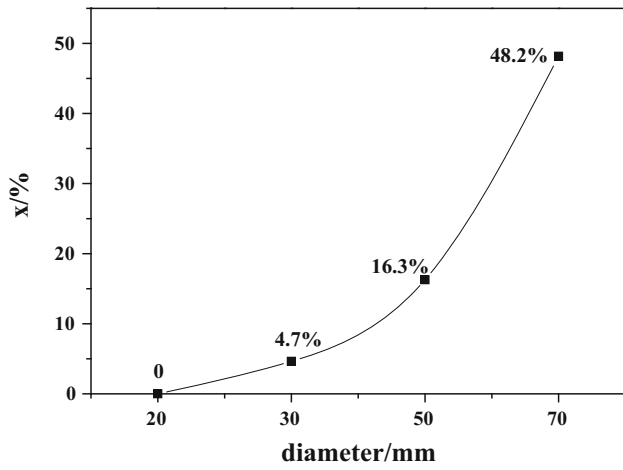


Fig.4—Average encapsulation parameters x for oxide–sulfide duplex inclusions in steel samples taken with different-sized samplers.

and the inclusions changed from oxide to oxide–sulfide duplex-type inclusions. Moreover, the solidification time of the steel increased with increasing sampler size, until a critical S content was reached, thereby triggering the formation of sulfide precipitates. Ohta *et al.*^[24–26] proposed that most sulfides precipitated at the end of solidification, which is in agreement with the results of this study. As shown in Figure 4, the encapsulation rates revealed that the amounts of oxide–sulfide duplex inclusion increased with increasing sampler size. The solidification velocity was calculated from the solidification time and secondary dendrite arm spacing of the steel^[27] as follows:

$$V = \frac{\lambda_2}{2t}, \quad [3]$$

where V ($\mu\text{m s}^{-1}$) is the velocity of the solidification front, λ_2 (μm) is the secondary dendrite arm spacing of the steel, and t (s) is the solidification time

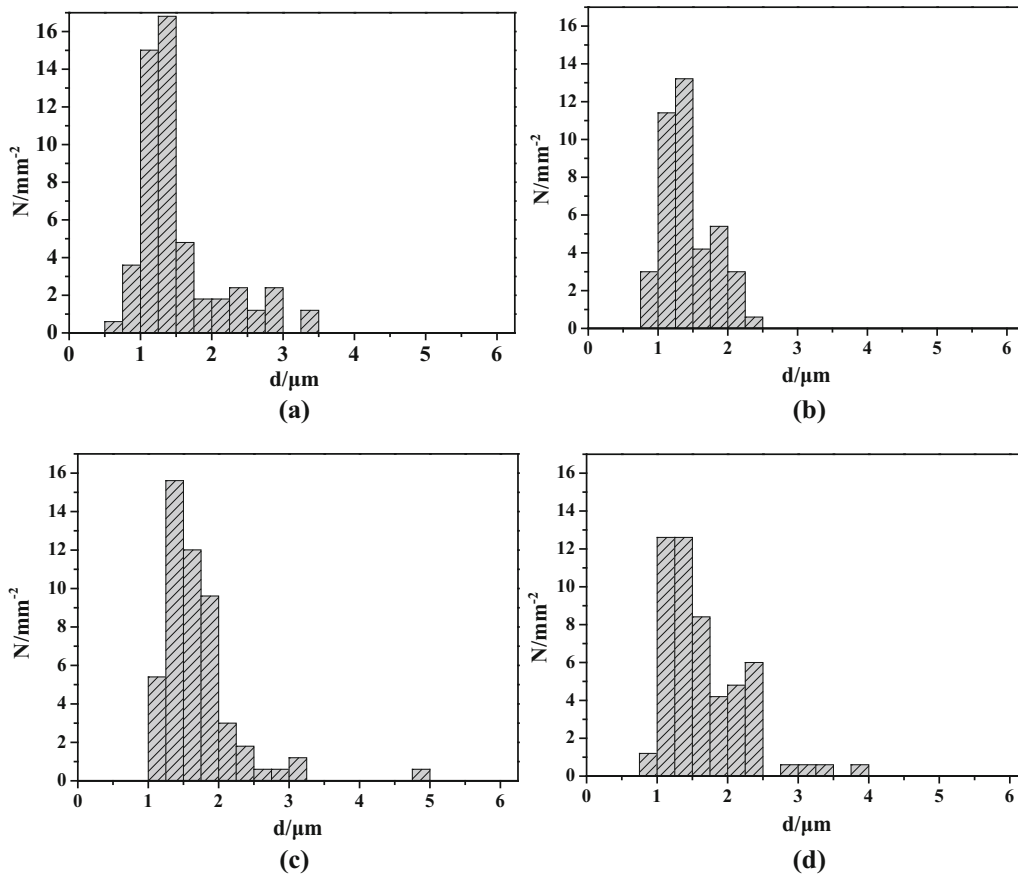
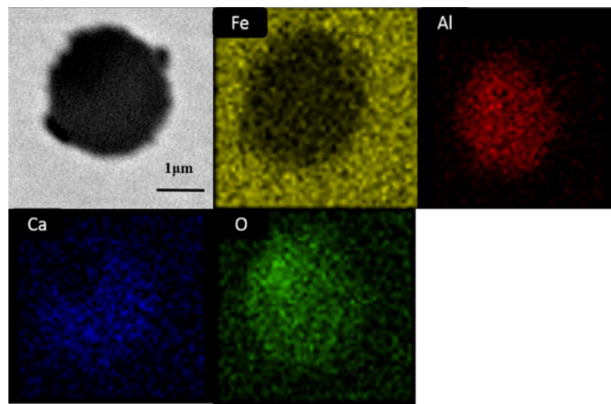


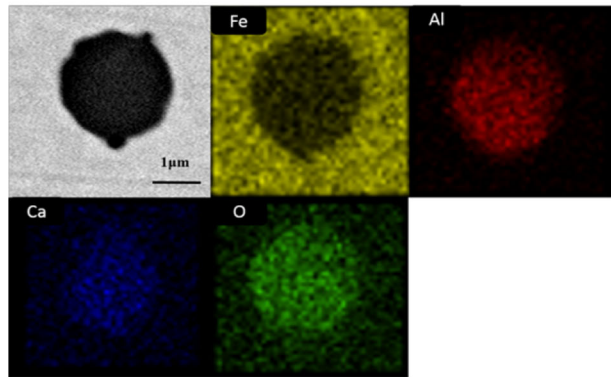
Fig. 5—Inclusion size distribution in steels obtained from barrel samplers with diameters of (a) 20 mm, (b) 30 mm, (c) 50 mm, and (d) 70 mm.

Table IV. Parameters of Inclusion Used in this Study

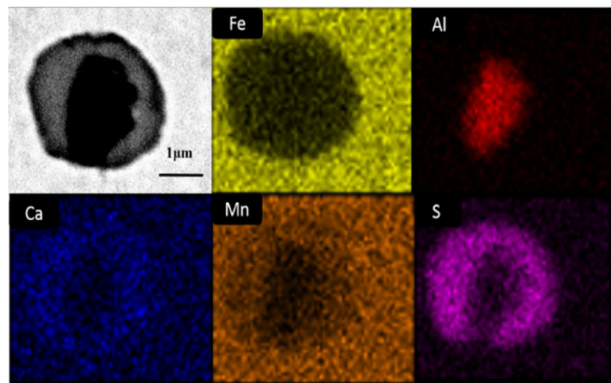
Parameter Value	$\gamma_{\text{PL}}/\text{mJ s}^{-2}$	$\gamma_{\text{PL}}/\text{mJ s}^{-2}$	$\gamma_{\text{PL}}/\text{mJ s}^{-2}$	a_0/m	$\eta/\text{Pa s}^{-1}$	$K_p/\text{W m}^{-1} \text{K}^{-1}$	$K_L/\text{W m}^{-1} \text{K}^{-1}$
	2290	2480	260	2.5	0.0043	5.5	45



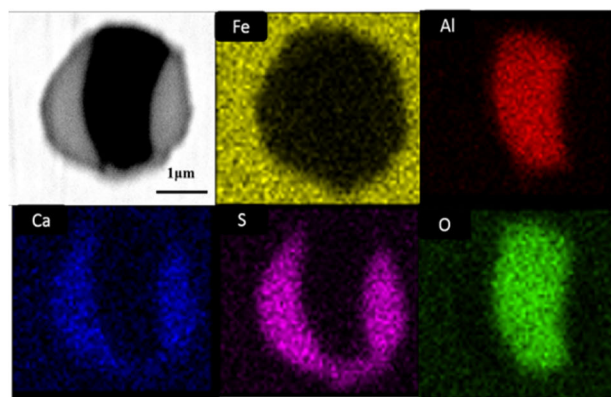
(a)



(b)



(c)



(d)

◀ Fig. 6—Scanning electron microscopy images and elemental energy-dispersive spectroscopy maps of inclusions in steel sampled by samplers with diameters of (a) 20 mm, (b) 30 mm, (c) 50 mm, and (d) 70 mm.

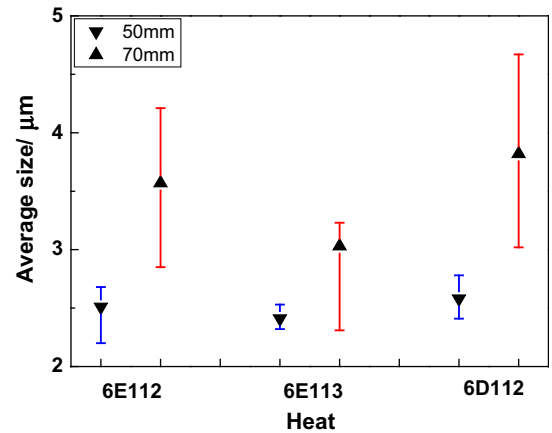


Fig. 7—Average size of sulfide inclusions in steel sampled by 50- and 70-mm-diameter samplers for of three heats.

($t = \Delta T/C_R$, where ΔT was 200 K (73 °C)^[21] and C_R was obtained from Eq. [2]). The calculated values of V were $3.7 \mu\text{m s}^{-1}$ (Group 1), $2.8 \mu\text{m s}^{-1}$ (Group 2), $1.4 \mu\text{m s}^{-1}$ (Group 3), and $0.2 \mu\text{m s}^{-1}$ (Group 4), respectively, as shown in Table III.

The critical velocity for particle engulfment and the pushing transition has been theoretically derived by Stefanescu *et al.*^[28,29] and is given as follows:

$$V_{cr} = \left(\frac{(\gamma_{PS} - \gamma_{PL})a_0^2}{3\eta kR} \right)^{1/2}, \quad [4]$$

where V_{cr} ($\mu\text{m s}^{-1}$) is the critical velocity for particle engulfment and pushing transition, γ_{PS} (mJ m^{-2}) is the interfacial energy between the particle and solid Fe, γ_{PL} (mJ m^{-2}) is the interfacial energy between the particle and liquid Fe, a_0 (m) is the atomic distance, η ($\text{kg m}^{-1} \text{s}^{-1}$) is the viscosity of liquid Fe, R (μm) is the particle radius, and k is the ratio of k_P/k_L , where k_P ($\text{W m}^{-1} \text{K}^{-1}$) and k_L ($\text{W m}^{-1} \text{K}^{-1}$) are thermal conductivities of the oxide particle and liquid Fe, respectively.

The inclusion size distribution in the steel obtained from the bottoms of the different-sized samplers (Figure 1) is shown in Figure 5. Most of the inclusions in this study had sizes ranging from 1 to 2 μm and corresponding critical velocities of 2.8–3.9 $\mu\text{m s}^{-1}$, which were obtained by substituting the parameters^[30] in Table IV into Eq. [4]. In the case of the Group 4 samples, the solidification velocity ($0.2 \mu\text{m s}^{-1}$) of the samples based on Eq. [3] was lower than the critical value and, therefore, all oxides should theoretically be encapsulated by sulfides; however, this group consisted of many single-phase oxides and, hence, more studies

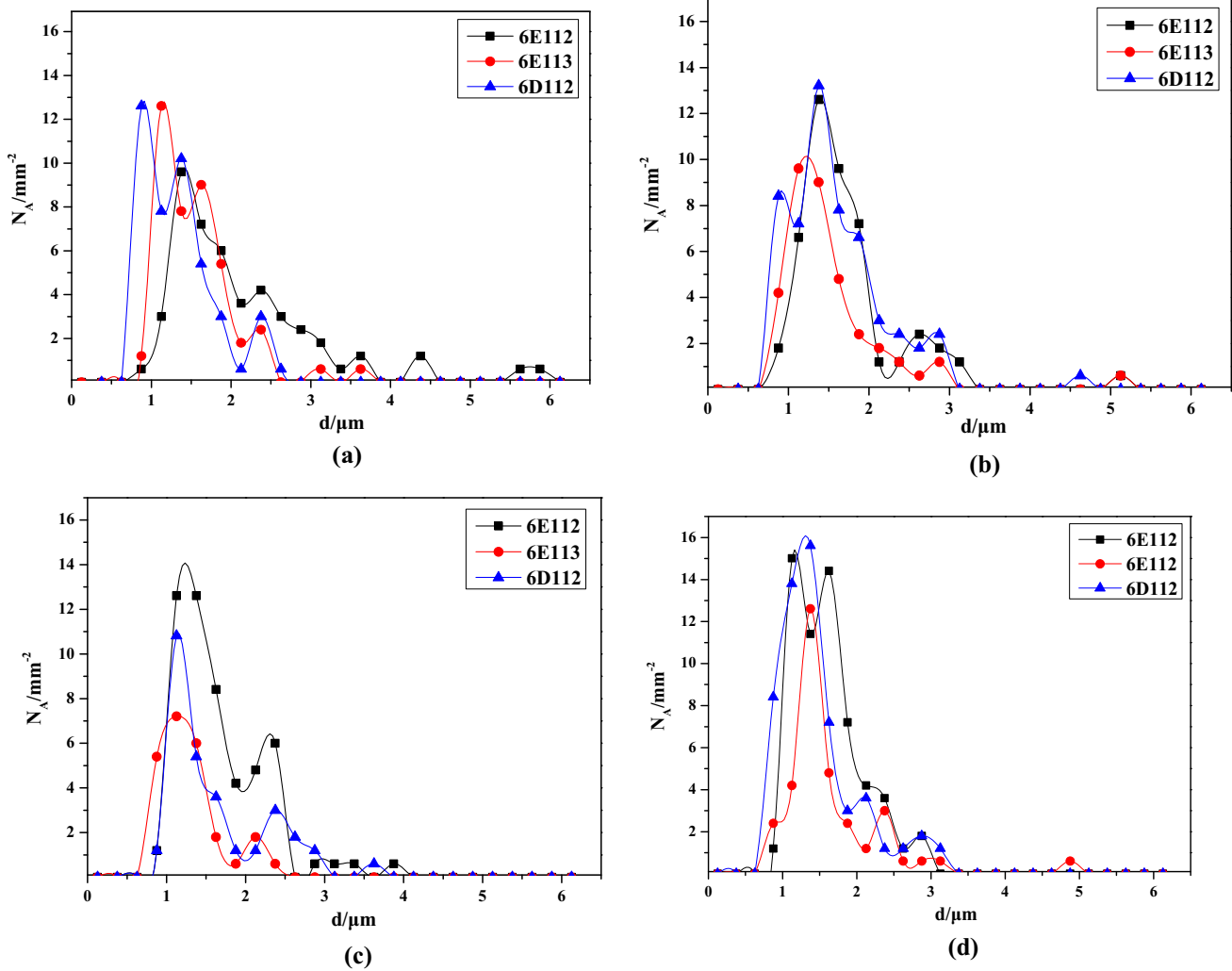


Fig.8—Size distribution of inclusions in steel samples taken from different positions of 70-mm-diameter steel sampler for three heats at (a) top, (b) center middle, (c) bottom, and (d) side middle locations of the sampler.

are required to fully understand the precipitation of sulfide on the oxides during solidification.

C. Inclusion Type in Different-Sized Steel Samples

Figure 6 shows SEM images of typical inclusions in the steel samples. The cooling rate of the steel had a strong influence on the compositions of inclusions. The major inclusions in the steels with cooling rates of 41.2 and 26.7 K s^{-1} were calcium aluminates, steel with a cooling rate of 8.2 K s^{-1} exhibited predominantly $\text{Al}_2\text{O}_3 + (\text{Ca}, \text{Mn})\text{S}$ complex inclusions, and steel with a cooling rate of 1.0 K s^{-1} gave $\text{Al}_2\text{O}_3 + \text{CaS}$ complex inclusions. The sulfides probably precipitated during the solidification process because of the segregation of S. Hollppa^[31] proposed that sulfides were mainly precipitated during solidification and Choudhary^[32] proposed that CaS formed from the reaction between S and calcium aluminates during solidification.

D. Changes in Size of Sulfide Inclusions

In this study, industrial experiments were performed in a tundish. Because of the low oxygen content, the composition and size of the oxides remained almost constant. This section therefore focused on the influence of the sampler size on the size of the sulfide inclusions. It was known from the aforementioned results that there were few sulfide inclusions in steel samples taken using samplers with diameters of 20 or 30 mm, so this section focused only on the inclusions found in samples taken with samples of 50 and 70 mm diameters. Figure 7 shows the average size of sulfide inclusions in steel (diameters of 50 and 70 mm) for the three heats. An average size of 2.5 μm was obtained from analysis of inclusions in the 50-mm-diameter samples; however, average sizes of 3.6, 3.2, and 3.8 μm were obtained from the three heats corresponding to the 70 mm-diameter sampler. The time for sulfide precipitation during solidification therefore increased with increasing sampler size, leading to an increase in the size of the sulfide inclusions.

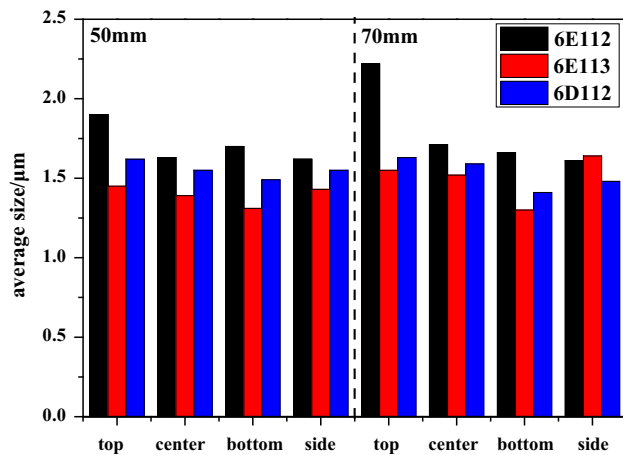


Fig.9—Average size of inclusions in steel samples taken from different positions of steel sampler with diameters of 50 and 70 mm for three heats.

E. Movement of Inclusions During Sampling Progress

To study the movement of inclusions during the sampling progress, the size distribution of the inclusions occurring at different positions of the steel samples was investigated. Because the sizes of the steel samples with diameters of 20 or 30 mm were too small, significant movement of inclusions was not apparent; therefore, this section focused on the movement of inclusions in the samples with the larger diameters. Four positions (top, bottom, center of the middle, and side of the middle) of these steel samples were examined.

Figure 8 shows the size distribution of inclusions at different positions of the 70-mm-diameter sample for the three heats. Figure 9 shows the average sizes of inclusions at the different positions of the steel sample (50 and 70 mm diameters) for the three heats. Figures 8 and 9 show that the size distribution of inclusions was greater and more dispersed from bottom to top. This may be attributed to the motion of liquid steel as it was poured into sampler, which caused collision and aggregation of the inclusions. In addition, the average sizes of inclusions in samplers taken from the centers and sides of the samplers showed no obvious differences, which meant that the inclusions did not spread significantly from the center to the surface of the sample. The main direction of inclusion movement was therefore upward during filling and solidification of the steel in the sampler.

IV. CONCLUSIONS

To determine the effect of different-sized samplers on the detection and analysis of inclusions in steel, four different-sized samplers were designed for industrial sampling from a tundish. The samples were evaluated via scanning electron microscopy and energy-dispersive spectroscopy. The results of this study are summarized as follows:

- (1) With increasing sample size, the cooling rate decreased and the encapsulation rate of complex inclusions increased from 0 to 48.2 pct. The velocity ($1.4 \mu\text{m s}^{-1}$) for particle engulfment and pushing transition of samples in the fourth group (samplers with diameter of 70 mm) was lower than the theoretically determined critical value, but not all oxides were encapsulated by sulfides.
- (2) The cooling rate of steel had a strong influence on the inclusion composition. The major inclusions in steels with cooling rates of 41.2 and 26.7 K s^{-1} were calcium aluminates, steel that cooled at 8.2 K s^{-1} exhibited mainly $\text{Al}_2\text{O}_3 + (\text{Ca}, \text{Mn})\text{S}$ complex inclusions, and steel produced at a cooling rate of 1.0 K s^{-1} gave $\text{Al}_2\text{O}_3 + \text{CaS}$ complex inclusions.
- (3) The average size of the sulfide inclusions increased with increasing size of the sampler. For example, the average sulfide diameter increased from 2.5 to 3.5 μm as the samplers inner diameters increased from 50 to 70 mm. The main direction of movement of the inclusions was upward during filling and solidification of the samples.
- (4) The inclusion size distribution, measured at different positions in the steel samples, indicated that there was no obvious difference between the average sizes of inclusions located in the center and side (of the middle), which meant that inclusions did not spread significantly from the center to the surface of the samples.

ACKNOWLEDGMENTS

This work was financially supported by the National Natural Science Foundation of China (Grant Nos. 51474085 and 51474076) and the Joint Projects of USTB and NTUT (Grant No. TW201604).

REFERENCES

1. H.C. Gao and X.H. Luan: *Sci. Technol. Baotou Steel*, 1996, vol. 1 (4), pp. 92–94.
2. W.J. Wang, X.H. Wang, and J.M. Zhang: *Contin. Cast.*, 2001, vol. 1 (2), pp. 25–27.
3. X.J. Li, D.Q. Zhou, and T. Hu: *Yeh Chin. Fen. His. Metall. Anal.*, 2001, vol. 21 (5), pp. 71–72.
4. Y.H. Zhang and S.Q. Li: *Tianjin Metall. T'ien-chin Yeh Chin*, 2003, vol. 1 (3), pp. 13–15.
5. Y.N. Wang, J. Yang, and Y.P. Bao: *Metall. Mater. Trans. B*, 2014, vol. 45B (6), pp. 2269–78.
6. K. Sakata and H. Suito: *Metall. Mater. Trans. B*, 1999, vol. 30B (6), pp. 1053–63.
7. Y.N. Wang, Y.P. Bao, and M. Wang: *Metall. Mater. Trans. B*, 2013, vol. 44B (5), pp. 1144–54.
8. F. Ruby-Meyer, A. Carré, and E. Hénault: *European Commission, Euro25039 EN*, 2012, p. 37.
9. O. Ericsson: D.D. Thesis. KTH, 2009.
10. Z. Zhang, A. Tilliander, A. Karasev, et al.: *ISIJ Int.*, 2010, vol. 50 (12), pp. 1746–55.
11. Z. Zhang, A. Tilliander, and M. Iguchi: *ISIJ Int.*, 2009, vol. 49 (10), pp. 1522–29.
12. L. Wang, S. Yang, and J. Li: *Metall. Mater. Trans. B*, 2016, vol. 47B (1), pp. 99–107.

13. Z.H. Chen, J.B. Yue, S.X. Luo, and X.L. Gan: *Ind. Metro.*, 2011, vol. S2, pp. 20–22.
14. Z. Ma and D. Janke: *ISIJ Int.*, 1998, vol. 38 (1), pp. 46–52.
15. H.T. Wang, Z.B. Xu, and F.M. Wang: *J. Univ. Sci. Technol. Beijing*, 2007, vol. 29 (9), pp. 884–89.
16. Z.Q. Li, L. Wu, and T. Liu: *J. Northeast. Univ. Nat. Sci.*, 2012, vol. 33 (9), pp. 1294–98.
17. M. Wintz, M. Bobadilla, and J. Lehmann: *ISIJ Int.*, 1995, vol. 35 (6), pp. 715–22.
18. H. Goto, K. Miyazawa, and K. Yamaguchi: *ISIJ Int.*, 1994, vol. 34 (5), pp. 414–19.
19. H. Goto, K. Miyazawa, and K. Tanaka: *ISIJ Int.*, 1995, vol. 35 (3), pp. 286–91.
20. H. Goto, K. Miyazawa, and H. Honma: *ISIJ Int.*, 1996, vol. 36 (5), pp. 537–42.
21. H. Ohta and H. Suito: *ISIJ Int.*, 2006, vol. 46 (1), pp. 22–28.
22. J.M. Cabrera-Marrero, V. Carreno-Galindo, and R.D. Morales: *ISIJ Int.*, 1998, vol. 38 (8), pp. 812–21.
23. M. El-Bealy and B.G. Thomas: *Metall. Mater. Trans. B*, 1996, vol. 27B (4), pp. 689–93.
24. H. Ohta and H. Suito: *ISIJ Int.*, 2006, vol. 46 (4), pp. 480–89.
25. H.M. Muhmond and H. Fredriksson: *Metall. Mater. Trans. B*, 2013, vol. 44B (2), pp. 283–98.
26. Y. Wang, S. Sridhar, and M. Valdez: *Metall. Mater. Trans. B*, 2002, vol. 33B (4), pp. 625–32.
27. H. Ohta and H. Suito: *ISIJ Int.*, 2006, vol. 46 (4), pp. 472–79.
28. D.M. Stefanescu and A.V. Catalina: *ISIJ Int.*, 1998, vol. 38 (5), pp. 503–05.
29. F.R. Juretzko, A.V. Catalina, and D.M. Stefanescu: *J. Jpn. Soc. Microgravity Appl.*, 1998, vol. 15, pp. 460–65.
30. S. Lei, M. Jiang, D. Yang, et al.: *J. Univ. Sci. Technol. B.*, 2013, vol. 11, pp. 1443–49.
31. L. Holappa, M. Hämäläinen, and M. Liukkonen: *Ironmak. Steelmak.*, 2003, vol. 30 (2), pp. 111–15.
32. S.K. Choudhary and A. Ghosh: *ISIJ Int.*, 2008, vol. 48 (11), pp. 1552–59.